Full-Time-Scale Power Management Strategy for Hybrid AC/DC/DS Microgrid with Dynamic Concatenation and Autonomous Frequency / Voltage Restorations

Qingzuo Meng, *Student Member, IEEE,* Pengfeng Lin, *Member, IEEE,* Yujie Wang, *Student Member, IEEE,* Miao Zhu, *Senior Member, IEEE,* Amer M. Ghias, *Senior Member, IEEE,* Syed Islam, *Fellow, IEEE,* Frede Blaabjerg, *Fellow, IEEE,*

Abstract—**Hybrid AC/DC/distributed energy storage (DS) microgrids (MGs) provide an effective solution for improving power accessibility and supply reliability in remote and isolated areas. Conventional static power management aims to proportionally allocate power based on unit ratings by scheduling the operation of interlinking converters (ILCs). Recent studies on transient power management emphasize inertia coupling among subgrids by dynamically regulating ILC power flows, thereby enhancing the system resilience against disturbances. In existing literature, these two objectives are normally addressed in a separate fashion and a unified scheme to simultaneously achieve them is rarely found. Furthermore, conventional static management neglects droop-induced frequency and voltage deviations which may seriously compromise the safe operation of sensitive loads. To address these limitations, in this paper, we proposes a full-time-scale (FTS) power management framework with dynamic concatenation and autonomous frequency/voltage restorations. Autonomous restoration controls are deployed in each subgrid to eliminate droop-induced frequency and voltage deviations, based on which a novel FTS dynamic concatenator is further proposed to chain up the static power sharing and transient inertia sharing across different time scales. Moreover, a novel global equivalent circuit model (GECM) is presented to interpret the holistic hybrid system from electrical circuit perspective. Then the static and transient performance of the complex hybrid AC/DC/DS MG can be quantitatively characterized to facilitate easier engineering practices. In-house experiments validate that the autonomous frequency/voltage restoration strategies effectively maintain the steady-state frequency /voltage of each subgrid at their respective nominal values, while the proposed FTS dynamic concatenator ensures static power sharing and transient inertia sharing through the ILC in full time scales.**

Index Terms—**Hybrid AC/DC/DS microgrids, full-time-scale power management, inertia transfers, static power management, autonomous frequency/voltage restoration**

I. INTRODUCTION

A. Research Background

Conventional power grids endure comparatively higher upfront costs and operating costs when they have to be extended and constructed in remote regions [1]–[3]. According to reports released by the International Energy Agency (IEA), due to limited access to main grids, there are still around 65 millions of people living on isolated islands in countries of Southeast Asia who cannot use

Corresponding author: Pengfeng Lin (Email: linpengfeng@ieee.org)

Qingzuo Meng, Pengfeng Lin, Yujie Wang, and Miao Zhu are with Shanghai Jiao Tong University, China.

Amer M. Ghias is with Nanyang Technological University, Singapore.

Syed Islam is with Federation University, Australia.

Frede Blaabjer is with Aalborg University, Denmark.

stable electricity. To meet basic needs of using electricity in these people, microgrids (MGs) can be built on islands spread widely in Southeast Asia regions and operated in island modes. In recent years, hybrid AC / DC / distributed energy storage (DS) MGs have gained increased attention as an effective paradigm to uniformly integrate energy storage systems into AC and DC subgrids [4].

A typical hybrid AC/DC/DS MG is illustrated in Fig. 1 and comprises four principal components: an AC subgrid, a DC subgrid, a DS subgrid, and an interlinking converter (ILC) that coordinates the power flows across subgrids. By integrating renewable energy sources (RES) such as photovoltaic (PV), wind, and small-scale hydro units into appropriate AC or DC subgrids, the hybrid MG can harness locally available resources with lower operational costs compared to pure AC or DC MGs. The DS subgrid further provides buffering and load balancing capabilities to mitigate the intermittency of RESs. In addition, ILC enables flexible power exchanges and coordinated dispatch for the entire hybrid MG, while is crucial to maintain the stability and reliability of the system [5], [6].

B. Literature Review and Gap Identifications

The integration of heterogeneous subgrids into hybrid AC/DC/DS MGs enables effective utilization of diverse RESs but comes with increasing system complexity, particularly in terms of static and transient power management. Static power management refers to global power sharing (GPS) under steady-state operating conditions. The core objective of GPS is to ensure all generation units in the hybrid system supply power to load demand proportionally to their capacities [7]. In contrast, transient power management intends to achieve that DERs with higher inertia buffer more of power demand in transient state, while those DERs with lower power density release power in a much slower way during the dynamic processes [8].

In light of static power management, for AC systems, each generation units are governed by frequency–power (f–P) droop. As there is only one frequency quantity in steady state, the locally measured frequency deviation by each generation can act as the coordination signal and drive the generator units to supply power commensurate with their capacity [9]. In this way, active power sharing in AC systems can be ensured. In contrast, DC systems lack a frequency state and therefore employ voltage–power (V–P) droop, in which bus voltage deviations help to imply the changes in load demands [10]. When it comes to the situation where AC and DC subgrids are bridged to form up a hybrid AC/DC system,
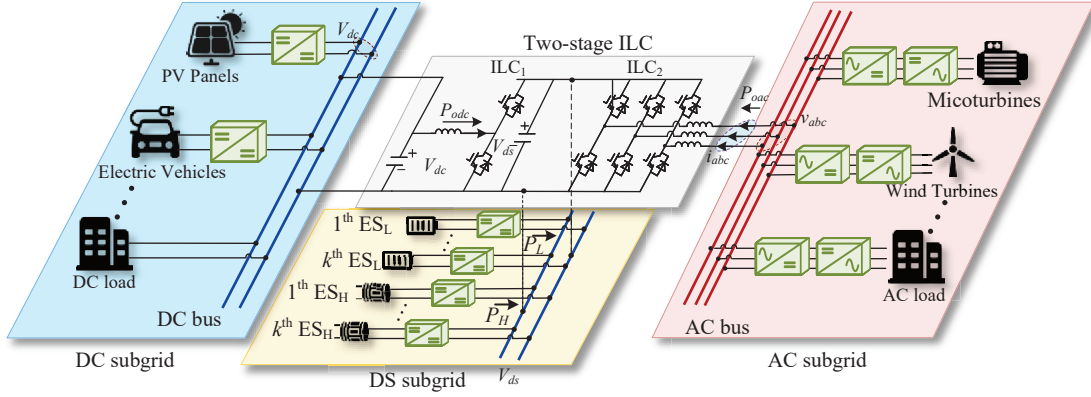
Fig. 1. System configuration of a typical hybrid AC/DC/DS MG.

as in reported [11], the per-unit (p.u.) values of AC frequency and DC voltage are utilized to indicate each subgrid's reserve margin. The p.u. values are then used to generate the power references for ILCs and coordinate inter-subgrid power exchanges. In this way, the global power sharing across the holistic hybrid MG can be achieved. In [12], a p.u. power-consistency term is incorporated into the model predictive control for ILCs, which equalizes the contribution levels across subgrids and ensures a global power sharing. In [13], a more advanced configuration involves connecting multiple ILCs in parallel to form an ILC community in the hybrid AC/DC MG. This configuration allows that each ILC in the community bears the power interaction between AC and DC subgrids in proportional to their capacity, thus to effectively avoid any possible power congestion between subgrids. Although the aforementioned static global power sharing control strategies guarantee proportional allocation with respect to subgrid capacities, it ineluctably leaves the transient behaviors of subgrids less attended.

As to dynamic power regulation, note that the extensive integration of low-inertia power electronic converters in hybrid AC/DC/DS MGs remarkably attenuates the system's overall inertia. This fact entails the hybrid MG system being susceptible to rapid load disturbances, which would result in steep frequency/voltage variations during transient periods [14]. Protective relays may then malfunction upon detecting high rate of change of frequency/voltage (RoCoF / RoCoV) incidents and precipitate the disconnection of RESs [15]–[17] . To tackle this issue, refs. [18] and [19] propose to modify the power control loop of ILC to enable transient power interactions between subgrids. The control methods fully the mobilize global inertia resources to cope with power fluctuations of loads and RESs. Ref. [20] introduces an ILC power control loop design which objective is to equalize the p.u. values of frequency / voltage rate of change in subgrids during system transition. By doing so, bi-lateral inertia support among AC and DC subgrids can be realized, and then transient performance of low-inertia subgrid can be considerably improved. However, it should be mentioned that all above research [18]–[20] provincially focus on dynamic inertia transfer, wherein a strong assumption is made that the normalized values of maximum allowable AC frequency (f) and DC / DS bus voltage (V_{dc} or V_{ds}) should be the same. This assumption, unfortunately, does not align with the condition of GPS in steady state, which means the dynamic power regulation and static GPS cannot be concurrently realized.

C. Motivations and Contributions

In fact, dynamic power regulation and static GPS take place at different time scales: the former happens in transient state while the later in steady state. No contradictions between the two objectives are observed and there should a way to smoothly string them. In the event of load step-up or step-down, transient inertia transfer is expected to occur first and subsequently, GPS can be attained at the end of load changes. Moreover, as demonstrated in [21], the deviations of f, V_{dc} or V_{ds} will not only impair frequency- and voltage-sensitive loads but may also induce system-wide instability. The synchronization with the utility grid also requires f_{ac}, V_{dc} and V_{ds} being driven to their nominal values as close as possible [21]. Responding to the needs of stringing dynamic and static power control objectives as well as mitigating the deviations of f, V_{dc}, V_{ds} in steady sate, a novel full-time-scale (FTS) power scheduling strategy for hybrid AC/DC/DS MGs is proposed. In this strategy, a FTS dynamic concatenator is proposed to chain up the objectives of dynamic and static power regulations at distinctive time scales. Autonomous frequency frequency/voltage restoration controls for AC, DC, and DS subgrids are actively consolidated into the respective control loops of the main power sources in individual subgrid, without compromising FTS power scheduling at all. The contributions of this paper are summarized as follows.

- Departing from conventional hybrid AC/DC/DS MG configurations [22], [23], a hybrid energy storage system (HESS) is proposed to replace the traditional single energy storage unit in the DS subgrid. The HESS is composed of different energy storages (ES) that can be classified into a cluster of low ramp rate ES (ES_L) and a cluster of high ramp rate ES (ES_H). Integral droop (ID) and traditional $V-P$ droops are applied to ES_H and ES_L. ES_Hs respond to high-frequency components of load fluctuations, whereas ES_Ls compensate for low-frequency ones. This method not only makes full use of the various advantages of different ESs, but also coordinates HESS as a whole to work as a DC generator. In this way, the HESS in DS subgrid can be dispatched to uniformly provide inertia supports to AC / DC subgrids and enhance the control flexibility of overall system.
- A FTS dynamic concatenator is proposed to reconfigure the ILC's power control loops accommodating different transient and static behaviors of all subgrids. The dynamic concatenator is arguably reported in this paper for the first time. It makes a breakthrough that enables seamless concatenation of global

transient inertia transfer to static power sharing, thereby achieving the intended power scheduling across the hybrid MG in full time scale.

- A steady-state autonomous frequency/voltage restoration control strategy is proposed to compensate for the steady-state deviations of f, V_{dc}, and V_{ds} introduced by droop controls. DC and DS bus voltages as well as AC frequency (as seen in Fig. 1) are autonomously restored to their nominal values. Thus, the risk of devices and sensitive loads dysfunction induced by large frequency and voltage deviations can be mitigated.

- A unified modeling approach for transient and static power management is proposed. In the approach, AC, DC, and DS subgrids are represented by Thévenin equivalent circuit models (ECMs). Three models are subsequently consolidated to a global equivalent circuit model (GECM) to characterize the entire hybrid AC/DC/DS MG. The proposed GECM provides insights to uniformly quantify the transient inertia transfer and static GPS in merely one dynamic model, with the FTS power scheduling and autonomous frequency/voltage restorations. This maneuver definitely lowers down the barriers for engineering practitioners to better dispatch inertia and power generations throughout the hybrid system.

The remainder of this paper is structured as follows: Section II discusses the configuration of hybrid AC/DC/DS MGs and the proposed control strategies. Section III presents the equivalent circuit models that elucidates the unified characterization of transient and static power management, with frequency/voltage autonomous restoration involved in each subgrid's control strategy. Sections IV and V verifies the feasibility and effectiveness of the proposed FTS power scheduling method by experiments. Finally, Section V concludes this paper.

II. CONFIGURATION AND CONTROL STRATEGIES OF HYBRID AC/DC/DS MGS

A. Hybrid AC/DC/DS MG Configuration

Fig. 1 illustrates the configuration of a typical hybrid AC/DC/DS MG. DC-based RESs and loads where the PVs and DC charging stations are integrated into DC subgrid, whereas AC-based sources including microturbines and wind turbines are connected to AC subgrid. The architecture that directly matches DC-output RESs with DC loads and AC-output RESs with AC loads effectively reduces the intermediate energy conversion stages and improves entire system efficiency [22]. A two-stage ILC consisting of a DC/DC converter (ILC_1) and a DC/AC converter (ILC_2) is deployed between AC and DC subgrids to manage the power transfer across subgrids. A DS subgrid, composed of a hybrid energy storage system, is integrated into the bus between ILC_1 and ILC_2 to buffer power imbalances incurred in AC and DC subgrids.

B. Virtual Inertia Control of AC, DC, and DS Subgrids

RESs are usually interfaced to hybrid AC/DC/DS MG via power electronic converters that inherently lack of inertia response capability. This causes system frequency and voltage to experience salient transient deviations under load disturbances. To tackle this challenge, a virtual inertia control is developed in [19], wherein the dynamic behavior of synchronous generators (SGs) is embedded
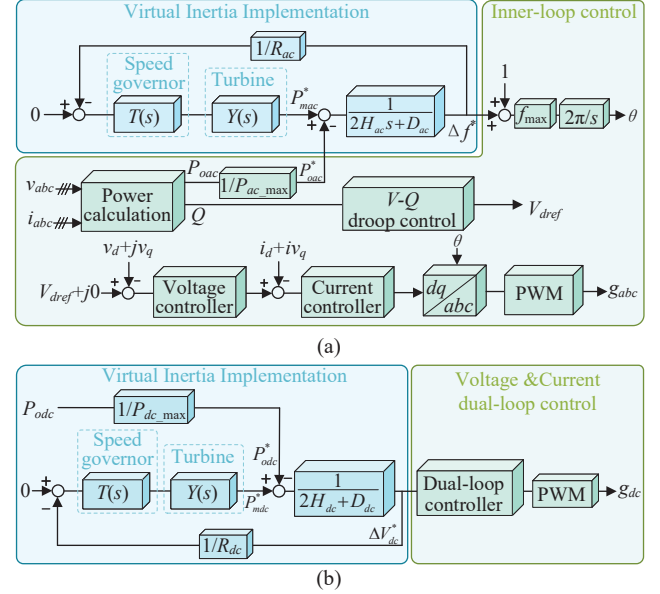

Fig. 2. Control diagrams of AC and DC subgrids. (a) DC subgrid. (b) AC subgrid.

into converter's control loops. As a result, the transient performance of system frequency and voltage can be strengthened without relying on rotor inertia of synchronous motor. Fig.2 (a) shows the virtual inertia-based control block diagram of AC subgrid, where $T(s)=1/(T_G s+1)$, refers to the transfer function of speed governor, while $Y(s)=(F_{HP}T_{RH}s+1)/[(T_{CH}s+1)(T_{RH}s+1)]$, represents the transfer functions of turbine in SGs. F_{HP}, T_{CH} and T_{RH} are time constants. P_{oac} and P_{ac_max} represent actual output power and the power capacity of AC subgrid, respectively. R_{ac} refers to the droop coefficient and g_{abc} defines gate signals for inverters in AC subgrids, respectively. In order to uniformly study the frequency regulation characteristics of SGs or converters with different rated powers, virtual inertia control is implemented in per unit (p.u.) domain [24]. For clarity, the prefix 'Δ', subscript 'max', and subscript '*' are employed to differentiate the change, maximum, and p.u. value of electrical quantities here and onwards.

In Fig. 2 (a), the inertia and damping block constitute the classical swing equation, which characterizes the dynamics of frequency regulation of SGs. Its dynamic model is provided as follows,

$$P_{mac}^* - P_{oac}^* = 2H_{ac}\frac{\mathrm{d}\Delta f^*}{\mathrm{d}t} + D_{ac}\Delta f^* \tag{1}$$

where H_{ac} represents the inertia coefficient, while D_{ac} signifies the damping coefficient of AC subgrid. P_{mac}^* and P_{oac}^* represent p.u. mechanical input power and output power, respectively. Δf^* means p.u. frequency change. As shown in (1), a high inertia coefficient moderates RoCoF ($\mathrm{d}\Delta f^*/\mathrm{d}t$) under abrupt load fluctuations.

In addition to its applications in AC systems as mentioned above, virtual inertia control can also be extended to DC systems to enhance the transient performance of DC bus voltage [19]. Fig. 2(b) shows the virtual inertia-based control block diagram of DC subgrid. The dynamic model of DC bus voltage is as follows,

$$P_{mdc}^* - P_{odc}^* = 2H_{dc}\frac{\mathrm{d}\Delta V_{dc}^*}{\mathrm{d}t} + D_{dc}\Delta V_{dc}^* \tag{2}$$

where H_{dc} represents the inertia coefficient, while D_{dc} signifies the damping coefficient of DC subgrid. P_{mdc}^* and P_{odc}^* represent
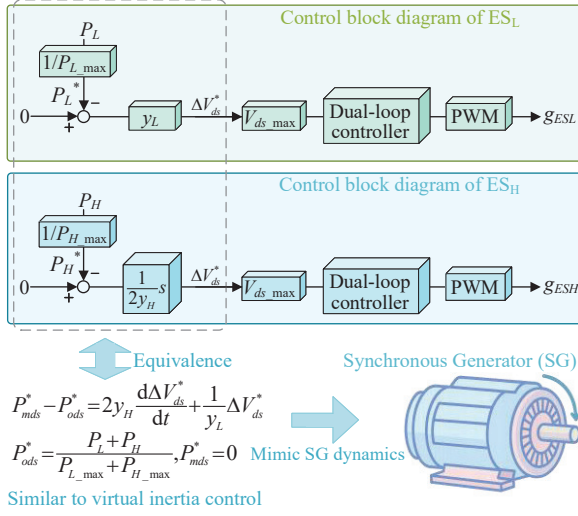
Fig. 3. Control block diagrams of ES$_L$ and ES$_H$ and their analogy with the swing equation of a synchronous generator.

p.u. mechanical input power and output power, respectively. ΔV_{dc}^* is p.u. DC bus voltage change. As virtual inertia control in both AC and DC subgrids has been extensively reported, more detailed explanations can be found in [18]–[20].

Within the DS subgrid, ES$_L$ and ES$_H$ are coordinated such that they respond to different frequency components of load demand. Specifically, ES$_L$ handles the slowly varying portion of load power through conventional V–P droop control, as expressed in the following,

$$V_{ds}^* = V_{ds\_ref}^* - \frac{1}{y_L} P_L^* \tag{3}$$

where P_L^* refers to p.u. output power of ES$_L$ converter. y_L is the droop coefficient of ES$_L$ converter. V_{ds}^* and $V_{ds\_max}^*$ represent the p.u. output voltage and max output voltage of ES$_L$ converter, respectively.

In contrast to ES$_L$, ES$_H$ exhibits superior performance in handling high-frequency load components due to its faster dynamic response. To enable ES$_H$ to actively compensate for high-frequency load, an integral droop (ID) control strategy is employed, wherein the power term of the conventional V–P droop control is substituted by the integral of power [25]:

$$V_{ds}^* = V_{ds\_ref}^* - \frac{1}{2y_H} \int P_H^* dt \tag{4}$$

where P_H^* refers to p.u. output power of ES$_H$ converter. y_H is the ID coefficient of the ES$_H$ converter.

It is worth noting that ES$_H$ and ES$_L$ are connected in parallel to the DS bus. They share the same output voltage, which equals the DS bus voltage shown in Fig. 1. ES$_H$ and ES$_L$ are responsible for compensating high and low frequency components of the DS load power, respectively. As a result, the sum of their output powers should be equal to the total power demand of the DS subgrid, which is given in the following,

$$P_H + P_L = P_{ods} \tag{5}$$

Since the base values of P_H, P_L and P_{ods} are all the capacity of DS subgrid, the p.u. form of (5) is as follows,

$$P_L^* + P_H^* = P_{ods}^* \tag{6}$$

According to (3)–(6), the frequency domain expressions of P_L^* and P_H^* can be derived as,

$$\begin{cases} P_L^* = \frac{y_L/y_H}{s+y_L/2y_H} P_{ods}^* \\ P_H^* = \frac{s}{s+y_L/2y_H} P_{ods}^* \end{cases} \tag{7}$$

where s is Laplace operator.

It can be observed from (7) that the coordination of conventional V–P droop and ID control enables ES$_H$ and ES$_L$ to handle the high and low frequency components of DS subgrid load demand, thereby utilizing the advantages of different types ESs in terms of energy and power density.

By consolidating (3) and (4), the transfer function from DS subgrid p.u. output power P_{ods}^* to DS bus p.u. voltage change ΔV_{ds}^* can be derived as:

$$\frac{\Delta V_{ds}^*}{P_{ods}^*} = \frac{-1}{2y_H s + y_L} \tag{8}$$

The relationship between P_{ods}^* and ΔV_{ds}^* indicates that the integration of conventional V–P droop and ID intrinsically forms a dynamic frequency regulation pattern that is analogous to the swing equation of SGs, as illustrated in Fig. 3. Although the DS subgrid's control loop is not explicitly incorporate virtual inertia or damping modules, the ID indeed emulates inertia behaviors, while the conventional V–P droop introduces damping characteristics into DS subgrid.

C. Proposed Autonomous Frequency/Voltage Restoration Strategy for AC, DC, and DS subgrids

Due to the droop characteristics of subgrids, there are deviations in DC and DS bus voltage as well as AC frequency, with respect to their nominal values in steady-state. To avoid potential degradation or malfunction to critical equipment resulting from undesired frequency and voltage deviations [26], an autonomous frequency/voltage restoration strategy is proposed, as seen in Fig. 4. In this figure, $x \in \{f, V_{dc}, V_{ds}\}$, represents the measured value of frequency or bus voltage. $x_{max} \in \{f_{max}, V_{dc\_max}, V_{ds\_max}\}$, refers to the maximum value of x. $x_n^* \in \{f_n^*, V_{dcn}^*, V_{dsn}^*\}$, refers to p.u. nominal value of x. $P_{ox} \in \{P_{oac}, P_{odc}, P_{ods}\}$, defines the output power of each subgrid. P_{ox}^* refers to the p.u. value of P_{ox}. e_x is the error signal processed by proportional-integral (PI) controllers. k_{px} and k_{ix} are proportional and integral coefficients, respectively. x_{in} defines the inner loop reference value. $\delta x^* \in \{\delta f^*, \delta V_{dc}^*, \delta V_{ds}^*\}$, is p.u. compensation signal for x^*. As illustrated in Fig. 4, the PI controller gradually regulate errors to be zero by continuously generating compensation signals for virtual inertia control loops, to achieve autonomous restorations of frequency and voltage to their nominal values. As indicated by [27], PI control parameters k_{px} and k_{ix} can be intentionally set to small values. The PI control bandwidths are much lower than that of inertia response in each subgrid. During transient periods, the change in compensation term δx^* can be negligible compared with the transient variation Δx^*. δx^* has a negligible impact on the dynamic behavior of frequency and voltage. In this way, the intended tri-lateral inertia sharing among three subgrids would be maintained whereas no deviation of f, V_{dc}, and V_{ds} in steady state would be observed.
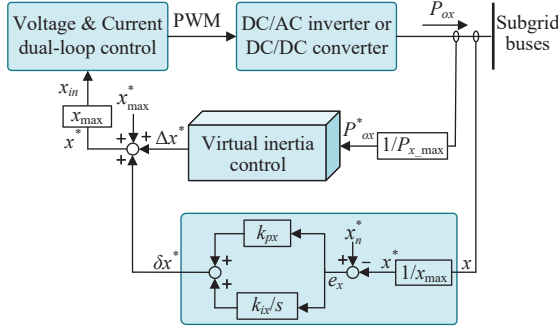
Fig. 4. Proposed autonomous frequency/voltage restoration controls for AC, DC, and DS subgrids. The virtual inertia control can be seen in Fig. 2 and Fig. 3.

D. Proposed Full-Time-Scale Dynamic Concatenator for Tow-Stage ILC

(1) **Control objective I: Transient tri-lateral inertia transfer to improve the dynamic response of low-inertia subgrids**

According to (1), (2), and (8), the changes of frequency and voltage Δx^* can serve as indicators of the subgrid inertia. For high-inertia subgrids, Δx^* changes comparatively slower during transients and exhibits a smaller dip. The two-stage ILC is then controlled to modulate inter-subgrid power exchange across all the subgrids so that Δx^* can always be kept the same in transient state. Therefore, transient disturbances happening to the entire hybrid MG would be primarily handled by high-inertia subgrids. The low-inertia subgrids experience the mitigated frequency/voltage excursions. This fact is equivalent to the partial transfer of inertia from high-inertia subgrids to low-inertia subgrids [18], [19].

Based on above reasoning, control objective I of ILC should be formulated as the following,

$$\text{Control objective I:} \quad \Delta f^* = \Delta V_{dc}^* = \Delta V_{ds}^* \qquad (9)$$

Given a particular subgrid where there are multiple distributed generation units, the quantity Δx^* is not identical among different units, which prevents the direct use of a unified Δx^* in control implementation. According to Fig. 4, $\Delta x^* = x^* - x_{\max}^* - \delta x^*$. x^* can be directly measured from the subgrid bus. $x_{\max}^*$ is a known constant. The frequency/voltage compensation term δx^* can be obtained from a central console. As explained earlier, it's control bandwidth is tuned far slower than inertia response and it can be seen as a constant [27]. In this sense, the control input to ILC is computed as $x^* - x_{\max}^* - \delta x^*$ which is equal to Δx^*. To facilitate theoretical derivations, the variable Δx^* is still adopted in the subsequent analysis.

To realize control objective I as in (9), the power control laws for ILC_1 and ILC_2 are given as,

$$\begin{cases} P_{1ref} = (\Delta V_{ds}^* - \Delta V_{dc}^*)G_{\text{PI1}} \\ P_{2ref} = (\Delta V_{ds}^* - \Delta f^*)G_{\text{PI2}} \end{cases} \qquad (10)$$

where P_{1ref} and P_{2ref} are power references of ILC_1 and ILC_2, respectively. G_{PI1} and G_{PI2} are PI controllers.

According to (10), the transient power regulation objective of ILC_1 aims to eliminate the imbalance between ΔV_{ds}^* and ΔV_{dc}^*. Given the high bandwidth of PI controller in the two-stage ILC, this imbalance quickly converges to zero. When DC subgrid experiences a load disturbance, ILC_1 actively redistributes part of load to DS subgrid to equalize the transient values of ΔV_{ds}^*

and ΔV_{dc}^*. A similar regulation occurs between the DS and AC subgrids through ILC_2, enabling the transient inertia transferring across the entire hybrid AC/DC/DS MG.

However, transient inertia transfer focuses on the transient state power distribution among subgrids; it fails to account for steady-state power coordination. As a result, subgrids with limited capacity may be forced to supply power beyond their rated limits, whereas those with larger capacity are just lightly loaded.

From Fig. 2 and Fig. 3, the transfer functions from p.u. output power of each subgrid to the corresponding p.u. frequency/voltage deviations can be derived. When $s \to 0$, these transfer functions characterize the steady-state relationship between the output power and frequency/voltage deviations given as,

$$\frac{\Delta f^*}{P_{oac}^*} = \frac{-R_{ac}}{D_{ac}R_{ac}+1}, \frac{\Delta V_{dc}^*}{P_{odc}^*} = \frac{-R_{dc}}{D_{dc}R_{dc}+1}, \frac{\Delta V_{ds}^*}{P_{ods}^*} = \frac{-1}{y_L} \quad (11)$$

The steady-state relations in (11) can be interpreted as the equivalent droop coefficients of each subgrid in p.u. domain. As reported in [18], droop equations are normally designed in SI domain so that the all distributed sources proportionally share the holistic load power. To ensure that droop coefficients are equivalent in two domains, the parameters R_{ac}, R_{dc}, and y_L in 11 should be carefully designed. The relation between the deviation of x and subgrid output power (P_{oac}, P_{odc}, P_{ods}) in SI domain can be listed below,

$$\begin{cases} \frac{\Delta f}{P_{oac}} = -\frac{f_{\max}-f_{\min}}{P_{ac\_\max}} \\ \frac{\Delta V_{dc}}{P_{odc}} = -\frac{V_{dc\_\max}-V_{dc\_\min}}{P_{dc\_\max}} \\ \frac{\Delta V_{ds}}{P_{ods}} = -\frac{V_{ds\_\max}-V_{ds\_\min}}{P_{ds\_\max}} \end{cases} \qquad (12)$$

where $P_{ac\_\max}$, $P_{dc\_\max}$, and $P_{ds\_\max}$ stand for the maximum output power of AC, DC, and DS subgrids. Converting (12) into its corresponding p.u. domain gives,

$$\begin{cases} \frac{\Delta f^*}{P_{oac}^*} = \frac{\Delta f/f_{\max}}{P_{oac}/P_{ac\_\max}} = -\frac{f_{\max}-f_{\min}}{P_{ac\_\max}}\frac{P_{ac\_\max}}{f_{\max}} \\ \frac{\Delta V_{dc}^*}{P_{odc}^*} = \frac{\Delta V_{dc}/V_{dc\_\max}}{P_{odc}/P_{dc\_\max}} = -\frac{V_{dc\_\max}-V_{dc\_\min}}{P_{dc\_\max}}\frac{P_{dc\_\max}}{V_{dc\_\max}} \\ \frac{\Delta V_{ds}^*}{P_{ods}^*} = \frac{\Delta V_{ds}/V_{ds\_\max}}{P_{ods}/P_{ds\_\max}} = -\frac{V_{ds\_\max}-V_{ds\_\min}}{P_{ds\_\max}}\frac{P_{ds\_\max}}{V_{ds\_\max}} \end{cases} \quad (13)$$

By means of parameter matching between (11) and (13), the following formulas hold,

$$\begin{cases} \frac{R_{ac}}{D_{ac}R_{ac}+1} = \frac{f_{\max}-f_{\min}}{f_{\max}} \\ \frac{R_{dc}}{D_{dc}R_{dc}+1} = \frac{V_{dc\_\max}-V_{dc\_\min}}{V_{dc\_\max}} \\ \frac{1}{y_L} = \frac{V_{ds\_\max}-V_{ds\_\min}}{V_{ds\_\max}} \end{cases} \qquad (14)$$

The expressions of R_{ac}, R_{dc}, and y_L can be further derived by rearranging (14), which are

$$\begin{cases} R_{ac} = \frac{f_{\max}-f_{\min}}{f_{\max}-D_{ac}(f_{\max}-f_{\min})} \\ R_{dc} = \frac{V_{dc\_\max}-V_{dc\_\min}}{V_{dc\_\max}-D_{dc}(V_{dc\_\max}-V_{dc\_\min})} \\ y_L = \frac{V_{ds\_\max}}{V_{ds\_\max}-V_{ds\_\min}} \end{cases} \qquad (15)$$

Referring to [24] and [19], D_{ac} and D_{ac} are commonly configured as 1 or 2. Then R_{ac} and R_{dc} can also be determined by (15) as the maximum and minimum values of frequency and voltages are normally known in system design phase.

It worth noting that the ILC control objective stipulated in (9) is merely for the tri-lateral inertia sharing among AC, DC, and DS subgrids during transient process. It does not cater to the desired

GPS in steady state. This fact be validated by combining (9), (11) and (14). In the case that the two-stage ILC only fulfill control objective I, the ratio of output power in three subgrids in steady state can be obtained as in (16) where $f_{\max}$, $V_{dc\_\max}$, and $V_{ds\_\max}$ are taken as base values.

$$
\begin{aligned}
P_{oac}^* &: P_{odc}^* : P_{ods}^* \\
&= \frac{f_{\max}}{f_{\max}-f_{\min}} : \frac{V_{dc\_\max}}{V_{dc\_\max}-V_{dc\_\min}} : \frac{V_{ds\_\max}}{V_{ds\_\max}-V_{ds\_\min}} \\
&= \frac{1}{1-f_{\min}^*} : \frac{1}{1-V_{dc\_\min}^*} : \frac{1}{1-V_{ds\_\min}^*}
\end{aligned}
\tag{16}
$$

It can be seen from (16) that GPS can be achieved only when the permissible p.u. deviation ranges of f, V_{dc}, and V_{ds} are identical. This requirement considerably hinders flexible system expansion and is too strict to be met in real applications.

(2) **Control objective II: Static global power sharing to ensure proportional power allocation among subgrids according to their respective ratings**

In steady state, the control objective of the ILC is to ensure that the output power of each subgrid is proportional to its maximum capacity, as shown in (17).

Control objective II: $\dfrac{P_{oac}}{P_{ac\_\max}} = \dfrac{P_{odc}}{P_{dc\_\max}} = \dfrac{P_{ods}}{P_{ds\_\max}}$ (17)

Owing to the droop characteristics of each subgrid, the steady-state values of f, V_{dc}, and V_{ds} deviate from their maximum values $f_{\max}$, $V_{dc\_\max}$, $V_{ds\_\max}$ when steady-state autonomous frequency/voltage restoration control is not employed. These deviations, as indicated in (18), directly reflect the loading conditions (LCs) of the corresponding subgrids. A larger LC signifies that the subgrid is more heavily loaded, whereas LC will increase in the case of light load [5], [6].

$$
\begin{cases}
LC_{ac} = \frac{f_{\max}-f}{f_{\max}-f_{\min}} \\
LC_{dc} = \frac{V_{dc\_\max}-V_{dc}}{V_{dc\_\max}-V_{dc\_\min}} \\
LC_{ds} = \frac{V_{ds\_\max}-V_{ds}}{V_{ds\_\max}-V_{ds\_\min}}
\end{cases}
\tag{18}
$$

where LC_{ac}, LC_{dc}, and LC_{ds} refer to LCs of AC, DC, and DS subgrids without steady-state recovery.

However, due to the existence of frequency/voltage restoration control strategy, the steady-state values of f, V_{dc}, and V_{ds} are strictly clamped at their nominal values. The consequent problem is that the loading situations of subgrids are no longer accessible. To tackle this issue, a relative loading index (RLI) inherited from [21] is presented to extract the hidden loading information after f, V_{dc}, and V_{ds} recovery. RLIs are defined as follows,

$$
\begin{cases}
RLI_{ac} = \frac{f_{\max}-f+\delta f}{f_{\max}-f_{\min}} \\
RLI_{dc} = \frac{V_{dc\_\max}-V_{dc}+\delta V_{dc}}{V_{dc\_\max}-V_{dc\_\min}} \\
RLI_{ds} = \frac{V_{ds\_\max}-V_{ds}+\delta V_{ds}}{V_{ds\_\max}-V_{ds\_\min}}
\end{cases}
\tag{19}
$$

where RLI_{ac}, RLI_{dc}, and RLI_{ds} refer to RILs of AC, DC, and DS subgrids with steady-state recovery. The main idea of RLI is to obtain the compensation term δx by the communication link and remove it's influence from the numerator of (18).

To realize control objective II, similar to (10), the power loop control laws of ILC_1 and ILC_2 are given below,

$$
\begin{cases}
P_{1ref}^* = (RLI_{dc} - RLI_{ds})G_{PI1} \\
P_{2ref}^* = (RLI_{ac} - RLI_{ds})G_{PI2}
\end{cases}
\tag{20}
$$

Retrospecting Fig. 4, the inertia response with frequency or voltage compensation term in each subgrid can be formulated as

$$
\begin{cases}
f = f_{\max} + \Delta f + \delta f \\
V_{dc} = V_{dc\_\max} + \Delta V_{dc} + \delta V_{dc} \\
V_{ds} = V_{ds\_\max} + \Delta V_{ds} + \delta V_{ds}
\end{cases}
\tag{21}
$$

Substituting (21) into (20), the control law of GPS can be reformed as follows,

$$
\begin{cases}
P_{1ref}^* = [(\frac{\Delta V_{ds}}{V_{ds\_\max}-V_{ds\_\min}})-(\frac{\Delta V_{dc}}{V_{dc\_\max}-V_{dc\_\min}})]G_{PI1} \\
P_{2ref}^* = [(\frac{\Delta V_{ds}}{V_{ds\_\max}-V_{ds\_\min}})-(\frac{\Delta f}{f_{\max}-f_{\min}})]G_{PI2}
\end{cases}
\tag{22}
$$

Equation (22) helps to explicitly unveil the relation between the changes in f, V_{dc}, V_{ds} and power references for ILCs. This will benefit the design of aforementioned FTS dynamic concatenator and be explained in subsequent context.

(3) **Proposed full-time-scale dynamic concatenator to string up objectives I and II**

As mentioned in Introduction, the two control objectives are realized at different time scales: the former happens in transient state while the later in steady state. There is no contradictions between them, which makes room for identifying a controller to accommodate them. However, existing studies typically address either transient inertia transfer or static global power sharing individually. Inertia transfer control alone unnecessarily fails GPS in steady state, whereas GPS related control strategy refrain from touching dynamic management during system transition. By scrutinizing (10) and (22), if the control objective of ILC follows (10) in transient stage and naturally degenerates to (22) as the system reaches steady state, tri-lateral inertia sharing and steady-state GPS can be smoothly realized without switching control laws. Based on the above reasoning, this paper proposes the FTS dynamic concatenator $T_x(s)$ to be as,

$$
T_x(s) = \frac{s + \omega_x}{s + \omega_0}
\tag{23}
$$

where ω_0 is the cutoff frequency of FTS dynamic concatenator. ω_x is defined as ω_{ac}, ω_{dc}, and ω_{ds} in AC, DC, and DS subgrids.

The specific design of ω_x is given as follows,

$$
\begin{cases}
\omega_{ac} = \frac{\omega_0 f_{\max}}{f_{\max}-f_{\min}} \\
\omega_{dc} = \frac{\omega_0 V_{dc\_\max}}{V_{dc\_\max}-V_{dc\_\min}} \\
\omega_{ds} = \frac{\omega_0 V_{ds\_\max}}{V_{ds\_\max}-V_{ds\_\min}}
\end{cases}
\tag{24}
$$

Fig. 5 illustrates the transient and static response characteristics of FTS dynamic concatenator. The p.u. variations of frequency or voltage (Δf^*, ΔV_{dc}^* or ΔV_{ds}^*) are fed into the FTS dynamic concatenator, of which the output values differs between the transient and steady-state stages. In the transient state (as s approaches infinity), the gain of the FTS dynamic concatenator is around unity. Therefore, its outputs are Δf^*, ΔV_{dc}^*, ΔV_{ds}^*. While in the steady state (as s approaches zero), the gain of the FTS dynamic are $\Delta f/(f_{\max}\text{-}f_{\min})$, $\Delta V_{dc}/(V_{dc\_\max}\text{-}V_{dc\_\min})$, and $\Delta V_{ds}/(V_{ds\_\max}\text{-}V_{ds\_\min\min})$. Based on the analyses from Fig. 5, the ILC control architecture depicted in Fig. 6 is formulated. It can be observed that FTS dynamic concatenator is positioned ahead of the PI controller within the ILC, so the power command generated by the PI controller follows (10) in transient stage and converges to (22) in steady stage. This effectively achieves the seamless transition between transient inertia transfer and static
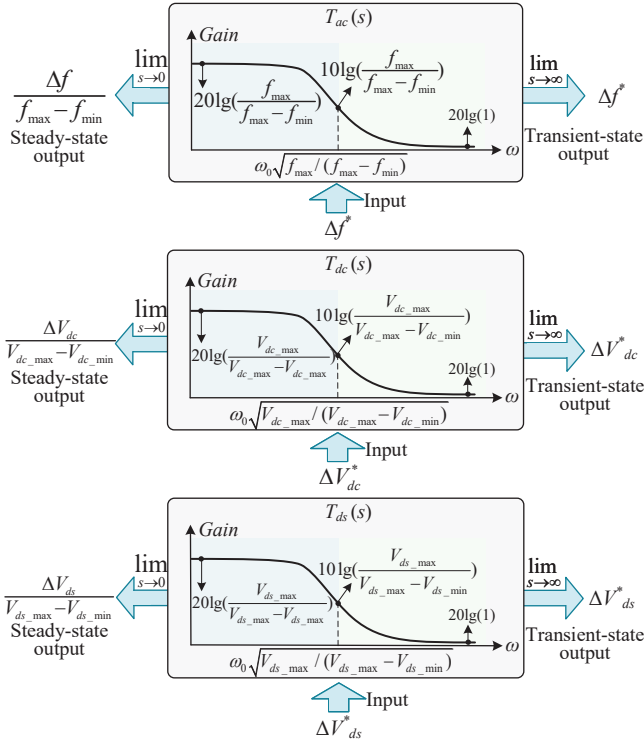
Fig. 5. Schematic diagram of transient and steady-state gain of FTS dynamic concatenator, which is positioned ahead of the power PI controller within the ILC. So the power command generated by the PI controller follows (10) in transient stage and converges to (22) in steady stage .
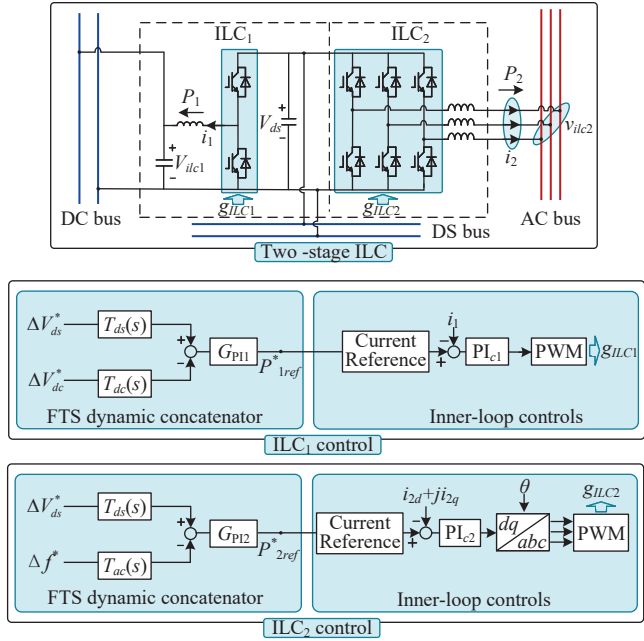

Fig. 6. Control block diagram of ILC with FTS dynamic concatenator.

GPS, thus to enhance both transient performance and subgrid's capacity utilization efficiency.

(4) **Parameter design for ω_0 in FTS dynamic concatenator**

Fig. 7 depicts Bode diagrams of $T_{ac}(s)$ under varying cutoff frequencies ω_0. It exemplifies the influence of ω_0 on FTS dynamic concatenator. The decrease in ω_0 extends the high-frequency band of the concatenator, which facilitates the transient inertia transfer.
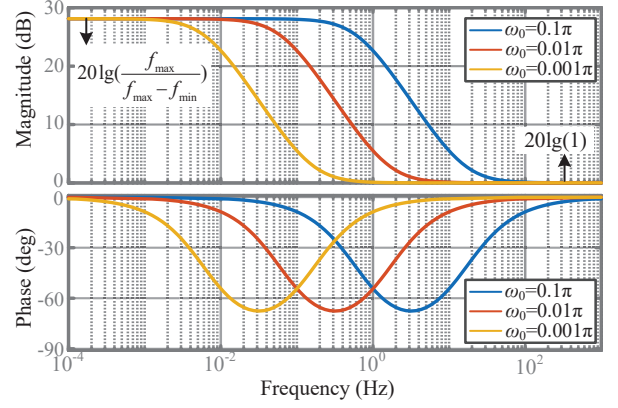

Fig. 7. Bode diagrams of $T_{ac}(s)$ with different cutoff frequencies ω_0.

However, ω_0 cannot be reduced indefinitely to an infinitely small value owing to numerical constraints of a digital signal processor (DSP). For the 32-bit floating-point DSP used in this work (TMS320F28335), it comprises one sign bit, eight exponent bits, and twenty-three bits forming the fraction [28]. The resulting minimum relative separation between adjacent numbers is as follow,

$$\varepsilon_{mach} = 2^{-23} \tag{25}$$

However, in real-time DSP computations, rounding and quantization errors accumulate through iterative updates of control states and interrupt latency. To ensure numerical stability under such conditions, an empirical safety factor M is introduced and define an effective numerical resolution ε.

$$\varepsilon = M\varepsilon_{mach} \tag{26}$$

In particular, when FTS concatenator is discretized with a sampling period T_s, the pole of it, $s = -\omega_0$, is mapped into the z domain as follow,

$$z_p = e^{-\omega_0 T_s} \tag{27}$$

For sufficiently small ω_0, the discrete pole approaches the unity circle, i.e.,

$$z_p \approx 1 - \omega_0 T_s \tag{28}$$

In finite-word-length DSP implementations, if $\omega_0 T_s \leq \varepsilon$, the pole is indistinguishable from unity and severe round-off errors or numerical instability may arise. Therefore, the following inequality must be satisfied by,

$$\omega_0 T_s \geq \varepsilon \Rightarrow \omega_0 \geq \frac{\varepsilon}{T_s} \tag{29}$$

For the DSP employed in this work, the sampling frequency is set to f_s=20 kHz, corresponding to a sampling period of T_s=50 μs. An empirical safety factor M is set to 1.3. Hence, the minimum value of ω_0 is $9.87 \times 10^{-4}\pi$, and ω_0 in this paper is specified as $1 \times 10^{-3}\pi$. This ensures the concatenator maintains its high-frequency inertia transfer while avoiding numerical issues in the DSP implementation.

III. PROPOSED GLOBAL EQUIVALENT CIRCUIT MODEL AND FULL-TIME-SCALE RESPONSE CHARACTERIZATION OF HYBRID AC/DC/DS MG

A. Proposed Global Equivalent Circuit Model

The transient and static performances of AC subgrid frequency, DC and DS subgrid bus voltages have been investigated in

previous sections. Section III characterizes the dynamic behavior of each subgrid by establishing its corresponding equivalent circuit model (ECM). The FTS dynamic concatenators given by (23) are also modeled as equivalent circuit elements. Furthermore, a global ECM (GECM) of the hybrid AC/DC/DS MG is constructed by used concatenator based elements to interconnect subgrid ECMs. The proposed GECM provides insights to uniformly quantify the transient tri-lateral inertia sharing and static GPS in merely one concise model where FTS power scheduling and autonomous frequency/voltage restorations are all accounted.

To analysze the response characteristics of different subgrids, expressions in (21) are transformed into p.u. forms as described in (30), which eliminates unit discrepancies arising from different physical quantities of voltage and frequency.

$$x^* = \frac{x_{\max}}{x_{\max}} + \frac{\Delta x}{x_{\max}} + \frac{\delta x}{x_{\max}} \Rightarrow x^* = 1 + \Delta x^* + \delta x^* \qquad (30)$$

The corresponding frequency domain expression of (30) is,

$$x^*(s) = 1/s + \Delta x^*(s) + \delta x^*(s) \qquad (31)$$

According to the control block diagrams of subgrids shown in Fig. 2 and Fig. 3, the transfer function from p.u. output power P_{ox}^* to p.u frequency/voltage x^* are as follows,

$$\begin{cases} \frac{\Delta f^*(s)}{P_{oac}^*(s)} = \frac{-R_{ac}}{(2H_{ac}s + D_{ac})R_{ac} + T(s)Y(s)} \\ \frac{\Delta V_{dc}^*(s)}{P_{odc}^*(s)} = \frac{-R_{dc}}{(2H_{dc}s + D_{dc})R_{dc} + T(s)Y(s)} \\ \frac{\Delta V_{ds}^*(s)}{P_{ods}^*(s)} = \frac{-1}{2y_H s + y_L} \end{cases} \qquad (32)$$

In (32), the base value of power in each subgrid is initially defined as its own maximum output power, leading to the p.u. output power P_{oac}^*, P_{odc}^*, and P_{ods}^*. Although this is convenient for describing local subgrid behavior, it complicates the analysis of power transfer among interconnected subgrids. Therefore, for subsequent system-level modeling, the power bases in (32) are unified and replaced by the total maximum capacity $P_{G\max}$ of the hybrid AC/DC/DS MG.

$$\begin{cases} \frac{\Delta f^*(s)}{P_{oac\_G}^*(s)} = \frac{-R_{ac}}{\frac{P_{ac\_max}}{P_{G\max}}(2H_{ac}s + D_{ac})R_{ac} + \frac{P_{ac\_max}}{P_{G\max}}T(s)Y(s)} = -Z_{ac}(s) \\ \frac{\Delta V_{dc}^*(s)}{P_{odc\_G}^*(s)} = \frac{-R_{dc}}{\frac{P_{dc\_max}}{P_{G\max}}(2H_{dc}s + D_{dc})R_{dc} + \frac{P_{dc\_max}}{P_{G\max}}T(s)Y(s)} = -Z_{dc}(s) \\ \frac{\Delta V_{ds}^*(s)}{P_{ods\_G}^*(s)} = \frac{-1}{\frac{P_{dc\_max}}{P_{G\max}}(2y_H s + y_L)} = -Z_{ds}(s) \\ P_{oac\_G}^*(s) = \frac{P_{oac}^*(s)P_{ac\_max}}{P_{G\max}}, \\ P_{odc\_G}^*(s) = \frac{P_{odc}^*(s)P_{dc\_max}}{P_{G\max}}, \\ P_{ods\_G}^*(s) = \frac{P_{odc}^*(s)P_{dc\_max}}{P_{G\max}}, \\ P_{G\max} = P_{ac\_max} + P_{dc\_max} + P_{ds\_max}. \end{cases} \qquad (33)$$

where $P_{G\max}$ is the total maximum capacity of the hybrid AC/DC/DS MG. $P_{ox\_G}^* \in \{P_{oac\_G}^*, P_{odc\_G}^*, P_{ods\_G}^*\}$ are p.u. output powers of three subgrids by re-normalizing the actual output powers with respect to the power base $P_{G\max}$.

Equation (33) can be uniformly expressed by,

$$\frac{\Delta x^*(s)}{P_{ox\_G}^*(s)} = -Z_x(s) \qquad (34)$$

wherein $Z_{ac}(s)$, $Z_{dc}(s)$, and $Z_{ds}(s)$ are collectively represented by Z_x. Substituting (34) into (30) gives the following expression,

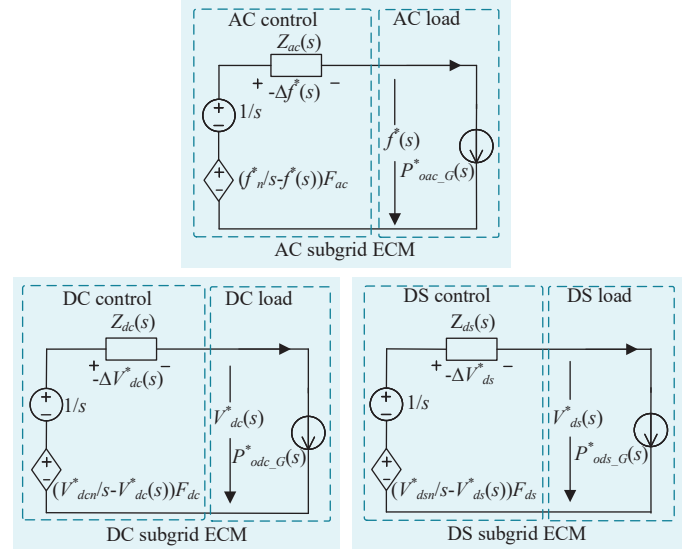$$x^*(s) = (1/s + \delta x^*(s)) - P_{ox\_G}^*(s)Z_x(s) \qquad (35)$$

Fig. 8. Equivalent circuit model of each subgrid.

where $(1/s + \delta x^*(s))$, $P_{ox\_G}^*(s)$, and $Z_x(s)$ are interpreted as open-circuit voltage, short-circuit current, and equivalent impedance, respectively. Then, equation(35) resembles the similar format of Thévenin equivalent circuit. Accordingly, ECMs depicted in Fig. 8 reveals the dynamic response characteristics of each subgrid from the circuit perspective, where $\delta x^*(s)$ is expressed by (36) according to the autonomous frequency/voltage control diagram in Fig. 4.

$$\delta x^*(s) = (x_n^*/s - x^*(s))F_x \qquad (36)$$

where $F_x = k_{px} + k_{ix}/s$, represents the transfer function of PI controller in frequency/voltage restoration controls.

In the hybrid AC/DC/DS MG, the two-stage ILC equipped with the FTS dynamic concatenator functions as the channel for inter-subgrid power exchange. This means the power exchanged through the ILC couples the dynamics of all three subgrids. Consequently, constructing a global ECM that captures the overall system dynamics requires an explicit circuit modeling of the ILC. According to Fig. 6, the dynamic characteristics of FTS dynamic concatenator can be converted into the following equivalent impedance.

$$\begin{cases} \frac{(T_{ds}(s)\Delta V_{ds}^*(s) - T_{dc}(s)\Delta V_{dc}^*(s))}{P_{1ref}^*(s)} = \frac{s}{k_{tp1}s + k_{ti1}} = Z_{\text{ILC1}}(s) \\ \frac{(T_{ds}(s)\Delta V_{ds}^*(s) - T_{ac}(s)\Delta f^*(s))}{P_{2ref}^*(s)} = \frac{s}{k_{tp2}s + k_{ti2}} = Z_{\text{ILC2}}(s) \end{cases} \qquad (37)$$

Assuming that $Z_{\text{ILC1}}(s)$ and $Z_{\text{ILC2}}(s)$ in (37) denote equivalent impedances, and $P_{1ref}^*(s)$ and $P_{2ref}^*(s)$ denote the corresponding equivalent currents, the impedance voltages $\Delta f^*(s)$, $\Delta V_{dc}^*(s)$, and $\Delta V_{ds}^*(s)$ can be interconnected through the equivalent impedances $Z_{\text{ILC1}}(s)$ and $Z_{\text{ILC2}}(s)$. In this way, the GECM of hybrid AC/DC/DS MG shown in Fig. 9 is obtained. In this figure, $P_{Lx\_G}^*(s) \in \{P_{Lac\_G}^*(s), P_{Ldc\_G}^*(s), P_{Lds\_G}^*(s)\}$ represents the local load power of the individual subgrid. All of subgrids' local load power are normalized with respect to the base value $P_{G\max}$. In the absence of ILC interconnection, the output power of each subgrid is solely determined by its local load demand. Through the interconnection by ILC, the output power of each subgrid is instead defined as the aggregation of its local load demand and the power from other subgrids.
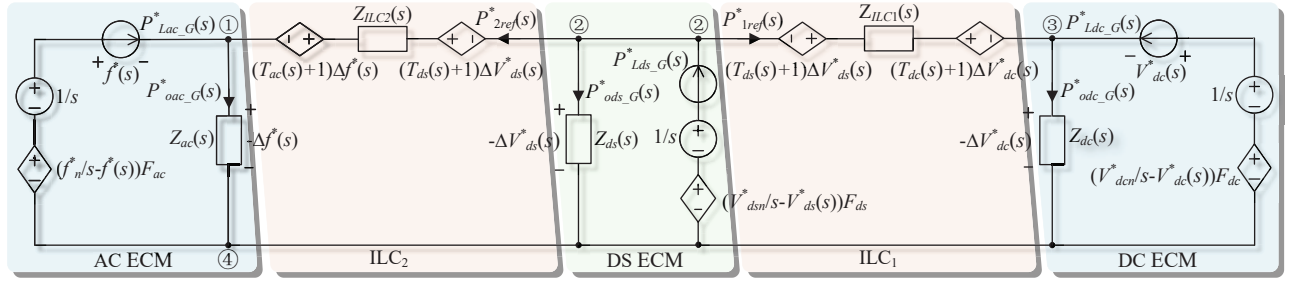
Fig. 9. Global equivalent circuit model of hybrid AC/DC/DS MG with FTS dynamic concatenator and frequency/voltage restoration control.

B. Full-Time-Scale Dynamic Analysis of Hybrid MG Base on the Proposed GECM

Note that Fig. 9 visualizes the dynamic response of hybrid AC/DC/DS MG through equivalent circuit representation. GECM of the entire hybrid MG can be modeled and solved by nodal analyses, as shown below,

$$GV_{node} = I_P \tag{38}$$

where G represents the node admittance matrix in Fig. 9. V_{node} denotes node voltage vector in which each element is the node voltage. I_P represents the vector in which each element is the current injecting into the node from current sources. The specifics of G, V_{node}, and I_P are given in (39).

In the following, the transient and steady-state characteristics of each subgrid's voltage or frequency, as well as the steady-state power characteristics, are further analyzed based on V_{node} and I_P obtained from (38) and (39).

(1) **Characterization of transient frequency / voltage responses and the analysis of bri-lateral inertia transfer scheme, based on Initial Value Theorem**

The transient inertia transfer mechanism can be revealed by comparing the inertia levels of each subgrid before and after the inertia sharing control is configured. According to (1), (2), and (8), it can be seen that $\Delta x^*(t)$ and $P_{ox}^*(t)$ are negatively correlated with the inertia coefficient. $\Delta x^*(t)/P_{ox}^*(t)$ attains its maximum absolute value when $t \to 0^+$. Consequently, $\Delta x^*(t)/P_{ox}^*(t)|_{t\to0^+}$ can serve as an indicator of the subgrid's inertia level. Accordingly, before the FTS dynamic concatenator is enabled, the inertia level of each subgrid can be represented by $\Delta x^*(t)/P_{ox}^*(t)|_{t\to0^+}$. Through Laplace transform, $\Delta x^*(t)/P_{ox}^*(t)|_{t\to0^+}$ can be represented in the Laplace domain as,

$$\begin{cases} \frac{\Delta f^*(t)}{P_{oac}^*(t)}\Big|_{t\to0^+} = \frac{\Delta f^*(s)}{P_{oac}^*(s)}\Big|_{s\to\infty} \\ \frac{\Delta V_{dc}^*(t)}{P_{odc}^*(t)}\Big|_{t\to0^+} = \frac{\Delta V_{dc}^*(s)}{P_{odc}^*(s)}\Big|_{s\to\infty} \\ \frac{\Delta V_{ds}^*(t)}{P_{ods}^*(t)}\Big|_{t\to0^+} = \frac{\Delta V_{ds}^*(s)}{P_{ods}^*(s)}\Big|_{s\to\infty} \end{cases} \tag{40}$$

To simplify the notation, let $\frac{\Delta f^*(s)}{P_{oac}^*(s)} = N_{ac0}(s)$, $\frac{\Delta V_{dc}^*(s)}{P_{odc}^*(s)} = N_{dc0}(s)$, and $\frac{\Delta V_{ds}^*(s)}{P_{ods}^*(s)} = N_{ds0}(s)$.

$N_{ac0}(s)$, $N_{dc0}(s)$, and $N_{ds0}(s)$ can an be directly obtained from the control block diagrams of the subgrids shown in Fig. 2 and

Fig. 3. Initial Value Theorem can then be applied to derive the inertia level of each subgrid without inertia sharing control,

$$\begin{cases} \lim_{s\to\infty} sN_{ac0}(s) = \lim_{s\to\infty} \frac{-sR_{ac}}{(2H_{ac}s+D_{ac})R_{ac}+T(s)Y(s)} = \frac{-1}{2H_{ac}} \\ \lim_{s\to\infty} sN_{dc0}(s) = \lim_{s\to\infty} \frac{-sR_{dc}}{(2H_{dc}s+D_{dc})R_{dc}+T(s)Y(s)} = \frac{-1}{2H_{dc}} \\ \lim_{s\to\infty} sN_{ds0}(s) = \lim_{s\to\infty} \frac{-s}{2y_Hs+y_L} = \frac{-1}{2y_H} \end{cases} \tag{41}$$

As shown in (41), applying Initial Value Theorem to (40) yields results related to the reciprocals of the inherent inertia of each subgrid. This means large inertia entails smaller deviations on frequency / voltage, and Initial Value Theorem in modern control theory can help to easily unveil inertia level in each subgrid.

After the proposed FTS dynamic connector is enabled, power exchange occurs among the subgrids. The frequency or voltage of each subgrid is influenced not only by its local load but also by the loads of other subgrids. In other words, load disturbances in any region of the hybrid AC/DC/DS MG are shared among all subgrids. Accordingly, with the FTS dynamic concatenator being enabled, the inertia level of each subgrid can be represented by $\Delta x^*(t)/P_{LG}^*(t)|_{t\to0^+}$, where P_{LG} is the total load power of the hybrid AC/DC/DS MG. Through Laplace transform, $\Delta x^*(t)/P_{LG}^*(t)|_{t\to0^+}$ can be represented in the Laplace domain as follows,

$$\begin{cases} \frac{\Delta f^*(t)}{P_{LG}^*(t)}\Big|_{t\to0^+} = \frac{\Delta f^*(s)}{P_{LG}^*(s)}\Big|_{s\to\infty} \\ \frac{\Delta V_{dc}^*(t)}{P_{LG}^*(t)}\Big|_{t\to0^+} = \frac{\Delta V_{dc}^*(s)}{P_{LG}^*(s)}\Big|_{s\to\infty} \\ \frac{\Delta V_{ds}^*(t)}{P_{LG}^*(t)}\Big|_{t\to0^+} = \frac{\Delta V_{ds}^*(s)}{P_{LG}^*(s)}\Big|_{s\to\infty} \\ P_{LG} = P_{Lac\_G} + P_{Ldc\_G} + P_{Lds\_G} \\ P_{LG}^* = \frac{P_{LG}}{P_{G\_max}} \end{cases} \tag{42}$$

To simplify the notation, let $\frac{\Delta f^*(s)}{P_{LG}^*(s)} = N_{ac1}(s)$, $\frac{\Delta V_{dc}^*(s)}{P_{LG}^*(s)} = N_{dc1}(s)$, and $\frac{\Delta V_{ds}^*(s)}{P_{LG}^*(s)} = N_{ds1}(s)$.

$N_{ac1}(s)$, $N_{dc1}(s)$, and $N_{ds1}(s)$ can an be obtained from (38). Based on this, Initial Value Theorem is applied to derive the inertia level index of each subgrid with inertia sharing control, as follows,

$$\begin{cases} N_{ac1}(s) = \frac{R_{ac}R_{dc}T_{ac}(s)T_{dc}(s)}{[R_{ac}R_{dc}(G_{ac}(s)+G_{dc}(s)+G_{ds}(s))+L(s)]} \\ N_{dc1}(s) = \frac{R_{ac}R_{dc}T_{ac}(s)T_{dc}(s)P_G(s)}{[R_{ac}R_{dc}(G_{ac}(s)+G_{oac}(s)+G_{ds}(s))+L(s)]} \\ N_{ds1}(s) = \frac{R_{ac}R_{dc}T_{ac}(s)T_{dc}(s)P_G(s)}{[R_{ac}R_{dc}(G_{ac}(s)+G_{dc}(s)+G_{ds}(s))+L(s)]} \\ G_{ac}(s) = (2H_{ac}s + D_{ac})T_{dc}(s)T_{ds}(s)P_{ac\_max}/P_{G\_max} \\ G_{dc}(s) = (2H_{dc}s + D_{dc})T_{ac}(s)T_{ds}(s)P_{ac\_max}/P_{G\_max} \\ G_{ds}(s) = (2y_Hs + y_L)T_{ac}(s)T_{ds}(s)P_{ac\_max}/P_{G\_max} \\ M(s) = R_{ac}T_{ac}(s)T_{ds}(s) + R_{dc}T_{dc}(s)T_{ds}(s) \\ L(s) = T(s)Y(s)M(s) \end{cases} \tag{43}$$

To ensure the implementation of inertia transfer, the PI controllers in the ILC power loop must react far more quickly than

$$G = \begin{bmatrix} \frac{1}{Z_{ac}(s)} - \frac{T_{ac}(s)}{Z_{\text{ILC2}(s)}} & \frac{T_{ds}(s)}{Z_{\text{ILC2}(s)}} & 0 \\ \frac{T_{ac}(s)}{Z_{\text{ILC2}(s)}} & \frac{1}{Z_{ds}(s)} - \frac{T_{ds}(s)}{Z_{\text{ILC1}(s)}} - \frac{T_{ds}(s)}{Z_{\text{ILC2}(s)}} & \frac{T_{ds}(s)}{Z_{\text{ILC1}(s)}} \\ 0 & \frac{T_{ds}(s)}{Z_{\text{ILC1}(s)}} & \frac{1}{Z_{dc}(s)} - \frac{T_{dc}(s)}{Z_{\text{ILC1}(s)}} \end{bmatrix},$$

$$V_{node} = \begin{bmatrix} -\Delta f^*(s) \\ -\Delta V_{ds}^*(s) \\ -\Delta V_{dc}^*(s) \end{bmatrix}, \quad I_P = \begin{bmatrix} P_{Lac\_G}^*(s) \\ P_{Lds\_G}^*(s) \\ P_{Ldc\_G}^*(s) \end{bmatrix}. \tag{39}$$

the intrinsic inertia response of each subgrid. This fast response is achieved by selecting sufficiently large proportional and integral gains k_{tpx} and k_{tix} of PI controllers in the ILC power loop. In this sense, (43) can be further expressed as follows,

$$\begin{cases} \lim_{s\to\infty} sN_{ac1}(s) = \frac{-1}{2H_G} \\ \lim_{s\to\infty} sN_{dc1}(s) = \frac{-1}{2H_G} \\ \lim_{s\to\infty} sN_{ds1}(s) = \frac{-1}{2H_G} \\ H_G = (H_{ac}\frac{P_{ac\_max}}{P_{G\_max}} + H_{dc}\frac{P_{dc\_max}}{P_{G\_max}} + y_H\frac{P_{ds\_max}}{P_{G\_max}}) \end{cases} \tag{44}$$

The inertia transfer mechanism of hybrid AC/DC/DS MG can be exemplified by comparing (41) and (44). H_G refers to a global inertia coefficient. It is derived by weighting the inherent inertia of each subgrid, where the weighting factor for each subgrid is the ratio of its maximum power capacity to the total system capacity. It should mentioned that the expression of H_G is the same as that of Center of Inertia (COI) in conventional power system [24]. This fact provides system operator with better understanding for the dynamic behavior of wide penetration of power electronics and they can somehow dispatch system inertia in their maturer way. As indicated by (44), inertia transfer control couples all subgrid dynamics. The inertia resources of all subgrids are pooled and collectively contribute to response to global load disturbances.

Fig. 10 illustrates Bode diagrams of $N_{ac0}(s)$ and $N_{ac1}(s)$ under a 60% load perturbation in subgrids. As shown in Fig. 10, the high-frequency magnitude of $N_{ac1}(s)$ is lower than that of $N_{ac0}(s)$. This reduction indicates the AC subgrid is supported by other subgrids with higher inertia through inertia transfer control. AC subgrid exhibits an increase in inertia level. Furthermore, when the integral gain y_H is increased from 7 to 15, the magnitude of $N_{ac1}(s)$ decreases even further in high frequency band. This trend demonstrates that a larger y_H effectively enhances the inertia level of the DS subgrid, and the inertia level of AC subgrid is further increased due to inertia transfer control.

(2) **Characterization of steady-state frequency / voltage and power outputs of the subgrids, based on Final Value Theorem**

Upon substituting $\Delta x^*(s)$ derived from (38) into (31), the steady-state responses of subgrid frequency and voltage can be directly analyzed via the Final Value Theorem.

$$\begin{aligned} x^*(t)|_{t\to\infty} &= \lim_{s\to 0} x^*(s)\,s \\ &= \left[\left(\frac{1}{s} + x_n^*(s)\right)/(1 + F_x(s)) - P_{ox\_G}^*(s)Z_x\right]s \\ &= x_n^* \end{aligned} \tag{45}$$

Equation (45) shows that the steady-state value of $x^*(t)$ autonomously converges to x_n^* due to existence of the proposed frequency/voltage restoration strategy in Section II Part C.
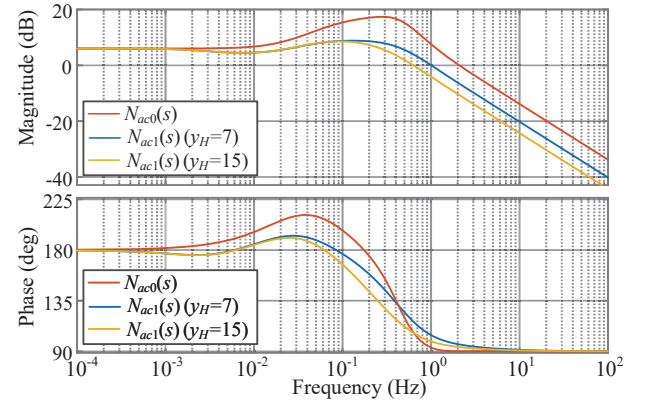

Fig. 10. Bode diagrams of $N_{ac0}(s)$ and $N_{ac1}(s)$ for AC sbugrid. $N_{ac0}(s)$ represents the frequency domain expression of $\Delta x^*(t)/P_{ox}^*(t)|_{t\to 0+}$ without FTS dynamic concatenator). $N_{ac1}(s)$ represents the frequency domain expression of $\Delta x^*(t)/P_{ox}^*(t)|_{t\to 0+}$ with FTS dynamic concatenator.
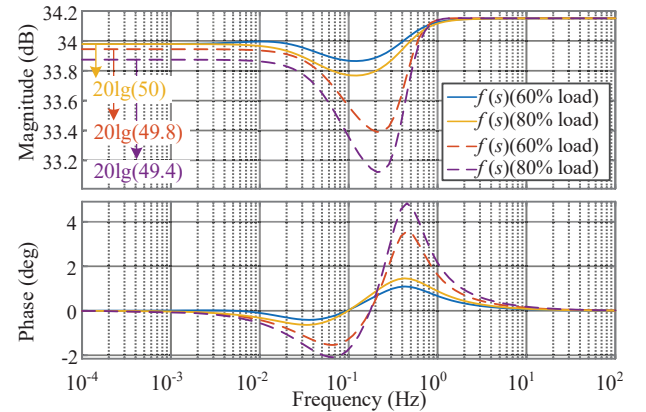

Fig. 11. Bode diagrams of $f(s)$ in AC subgrid with steady-state restoration (solid lines) and $f(s)$ without steady-state restoration (dotted lines).

As an example, Fig. 11 shows Bode diagrams for $f(s)$ with steady-state autonomous restoration (solid lines) and $f(s)$ without steady-state autonomous restoration (dashed lines). As observed from Fig. 11, with steady-state autonomous restoration, the low-frequency magnitude of f remains fixed at $20\lg(50)$ regardless of load variations. In contrast, without steady-state autonomous restoration, the low-frequency magnitude of $f(s)$ decreases progressively as the load increases.

According to (38), when the Z_{ILCn} is ignored, the p.u. output

power of each subgrid can be deduced as follows,

$$
\begin{cases}
P^*_{oac\_G}(s) = \frac{(T(s)\,Y(s)+D_{ac}R_{ac}+2H_{ac}R_{ac}s)R_{dc}T_{dc}(s)T_{ds}(s)}{G'_{ac}(s)+G'_{dc}(s)+G'_{ds}(s)} \\
P^*_{odc\_G}(s) = \frac{(T(s)\,Y(s)+D_{dc}R_{dc}+2H_{dc}R_{dc}s)R_{ac}T_{ac}(s)T_{ds}(s)P^*_{LG}(s)}{G'_{ac}(s)+G'_{dc}(s)+G'_{ds}(s)} \\
P^*_{ods\_G}(s) = \frac{R_{ac}R_{dc}T_{dc}(s)T_{ds}(s)(y_L+2y_Hs)P^*_{LG}(s)}{G'_{ac}(s)+G'_{dc}(s)+G'_{ds}(s)} \\
G'_{ac}(s) = G_{ac}(s)R_{ac}R_{dc} + R_{ac}T(s)\,Y(s)T_{ac}(s)T_{ds}(s) \\
G'_{dc}(s) = G_{dc}(s)R_{ac}R_{dc} + R_{dc}T(s)\,Y(s)T_{dc}(s)T_{ds}(s) \\
G'_{ds}(s) = G_{ds}(s)R_{ac}R_{dc}
\end{cases}
\tag{46}
$$

By first applying the Final Value Theorem to (46) and then substituting the result from (15), the steady-state output power of each subgrid is obtained.

$$
\begin{cases}
P^*_{oac\_G}(t)|_{t\to\infty} = \lim_{s\to} sP^*_{oac\_G}(s) = P_{ac\_max}\frac{P^*_{LG}}{P_{G\_max}} \\
P^*_{odc\_G}(t)|_{t\to\infty} = \lim_{s\to} sP^*_{odc\_G}(s) = P_{dc\_max}\frac{P^*_{LG}}{P_{G\_max}} \\
P^*_{ods\_G}(t)|_{t\to\infty} = \lim_{s\to} sP^*_{ods\_G}(s) = P_{ds\_max}\frac{P^*_{LG}}{P_{G\_max}}
\end{cases}
\tag{47}
$$

According to (47), the steady-state output powers of subgrids in the SI domain exhibit the following proportional relationship.

$$
\begin{aligned}
&P_{oac} : P_{odc} : P_{ods} \\
&= P^*_{oac\_G}P_{G\_max} : P^*_{odc\_G}P_{G\_max} : P^*_{ods\_G}P_{G\_max} \\
&= P_{ac\_max} : P_{dc\_max} : P_{ds\_max}
\end{aligned}
\tag{48}
$$

As established by (48), the actual output power of each subgrid is proportional to its maximum capacity in steady state, and GPS is therefore obtained.

IV. EXPERIMENTAL VERIFICATION

According to the system configuration shown in Fig. 1, hardware experiments were conducted in a hybrid MG to validate the effectiveness of proposed full-timescale power management and steady-state frequency/voltage autonomous restoration control strategy. TABLE I displays the system parameter configurations. The control algorithms were performed on a digital signal processor (DSP-TMS320F28335) together with a controller board. The DC bus was set up by a programmable DC power supply (Chroma 62100H-600S) via a droop-characterized DC/DC converter. The DC power supply (Magna-Power MTD1000-100/380) formed an AC subgrid through a DC/AC converter. ES_L and ES_H formed HESS and were connected to the DC capacitor of the two-stage ILC (a.k.a. DS bus). The power ratings of battery pack and supercapacitor pack are 14.4 kW and 5.6 kW.

Experimental waveforms were captured by a Tektronix MDO3000 Mixed Domain Oscilloscope and subsequently exported to MATLAB for further analysis of the system's transient response metrics. The RoCoV and RoCoF at the instant of a load disturbance were approximated by differentiating the voltage or frequency measurements at the disturbance instant and the immediately succeeding sampling point. In essence, $\Delta x^*(t)/P^*_{ox}(t)|_{t\to 0+}$ represents the rates of change of frequency and voltage (RoCoF / RoCoV) at the instant of a load disturbance. Leveraging the proposed GECM, the rates of change of p.u. AC frequency, DC voltage, and DS voltage after inertia transfer can be quantitatively calculated by (44). Performing the load disturbance, AC subgrid RoCoF, DC subgrid RoCoV, and DS subgrid RoCoV are computed as in Table II.

A. Hybrid Microgrid with Inertia Transfer but Without Frequency/Voltage Restoration Control

To assess the influence of the FTS dynamic concatenator and the frequency/voltage restoration control on the hybrid AC/DC/DS MG, Fig. 12 (a) depicts the dynamic responses of the hybrid AC/DC/DS MG with only transient inertia transfer are reported in [18], [19], while Fig. 12 (b) illustrates that DC, AC, and DS subgrids undergo load variations of 14 kW, 12 kW, and 10 kW at first. Upon the settlement of the initial perturbation, the load power of AC subgrid is subsequently raised by an additional 6 kW. As illustrated in Fig. 12 (a), the RoCoF of the AC subgrid and the RoCoV of DC and DS subgrids at the moment of the load disturbance are 27.32 V/s, 3.66 Hz/s, and 51.08 V/s, respectively, which aligns closely with the values reported in Table II. This concordance substantiates the capability of the global ECM to accurately quantify the system's effective inertia.

Owing to the absence of frequency and voltage restoration mechanisms, both quantities drift away from their nominal values following load disturbances. Under successive disturbances, the resulting frequency and voltage excursions may exceed permissible thresholds, thereby jeopardizing the secure and reliable operation of the hybrid MG. In addition, since the transient inertia transfer mechanism is fundamentally oriented toward enhancing the system's dynamic responsiveness while neglecting its steady-state power allocation, subgrids fail to attain a proportionate distribution of global system load in steady state, as illustrated in Fig. 12(b). This situation may drive certain subgrids beyond their permissible operating limits, whereas the available capacity margins of others remain substantially underutilized.

B. Hybrid Microgrid with FTS Dynamic Concatenator and Frequency/Voltage Restoration Control

Fig. 13 illustrates the dynamic responses of hybrid MG with the FTS dynamic concatenator and the frequency/voltage restoration control. A comparison between Fig. 12(a) and Fig. 13(a) reveals that the steady-state autonomous restoration control effectively maintains the DC bus voltage and AC frequency at their nominal values despite repeated load disturbances.

Fig. 13(b) illustrates that the DC, AC, and DS subgrids undergo load perturbations of 14 kW, 12 kW, and 10 kW during the initial disturbance, and subsequently stabilize at an identical steady-state output of 16 kW. When an additional 6 kW load is subsequently applied to the AC subgrid, the system maintains golbal power sharing. This result demonstrates that ILC equipped with the FTS dynamic connector can perform inertia sharing control during the transient phase and progressively transition to steady-state global power sharing control, thereby simultaneously ensuring favorable transient response performance and optimized steady-state power allocation.

Fig. 13(c) illustrates the output power of the ES_L and ES_H in HESS, where ES_L and ES_H actively handle low frequency and high frequency power, respectively. When the load change occurs, ES_H immediately responds to the rapid change in load power and then gradually decreases to zero, while the output power of ES_L slowly rises until it takes over all the load of DS subgrid. This result indicates that the coordinated control under conventional P–V and ID droop control strategies can effectively leverage

TABLE I
KEY SYSTEM PARAMETER SETTINGS

System Components	Parameter	Setting
AC subgrid	Input and output voltage	380 V, 710 V
	Maximum frequency	51 Hz
	Minimum frequency	49 Hz
	Nominal frequency	50 Hz
	Maximum output power	20 kW
	Inertia and damping coefficient	$H_{ac} = 2, D_{ac} = 1$
DC subgrid	Input voltage	100 V
	Maximum DC bus voltage	380 V
	Minimum DC bus voltage	370 V
	Nominal DC bus voltage	370 V
	Maximum output power	20 kW
	Inertia and damping coefficient	$H_{dc} = 3, D_{dc} = 1$
DS subgrid	Input voltage	250 V
	Maximum DS bus voltage	710 V
	Minimum DS bus voltage	690 V
	Nominal DS bus voltage	700 V
	Maximum output power	20 kW
	Traditional and integral droop coefficients	$y_H = 7.5, y_L = 0.0403$
Other parameters of virtual inertia	$T_G, F_{HP}, T_{CH}, T_{RH}$	0.1, 0.3, 0.2, 7

TABLE II
GLOBAL INERTIA COEFFICIENT H_G AND SUBGRID'S ROCOF/ROCOV FOR
VARIOUS ID COEFFICIENTS y_H BY GECM OF (44). (NOTE: DC, AC, AND DS
SUBGRIDS UNDERGO LOAD VARIATIONS OF 14 kW, 12 kW, AND 10 kW.)

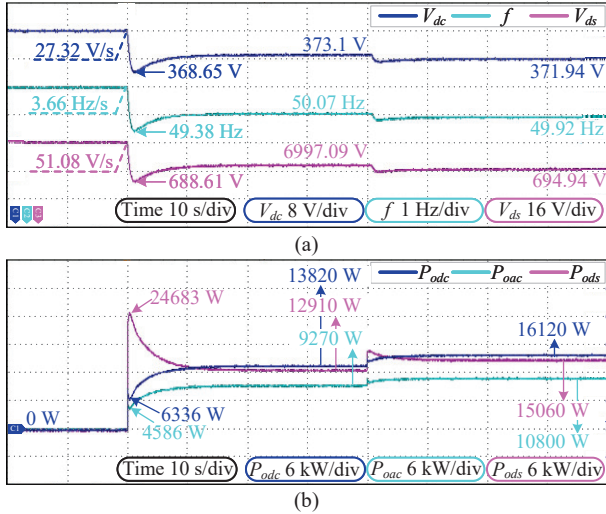| y_H	H_G	RoCoF of AC subgrid	RoCoV of DC subgrid	RoCoV of DS subgrid
15	12.5/3	3.67 Hz/s	27.36 V/s	51.12 V/s
30	20/3	2.29 Hz/s	17.10 V/s	31.95 V/s

Fig. 12. Response of hybrid MG with inertia transfer but Without frequency/voltage restorations. (a) DC bus voltage and AC frequency response. (b) Output power of DC and AC subgrid.
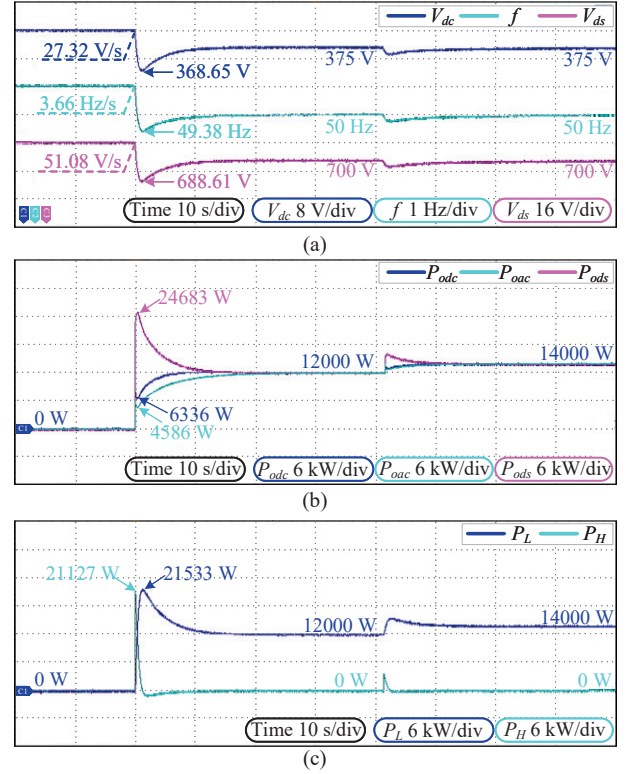
the respective advantages of high-power-density and high-energy-density energy storage systems.

Fig. 13. Response process of hybrid MG with FTS dynamic concatenator and frequency/voltage restoration control (y_H=15). (a) DC bus voltage and AC frequency response. (b) The output power of DC, AC and DS subgrid. (c) Power allocation of ES_L and ES_H in DS subgrid.

C. Increase the Integral Droop Coefficient y_H in DS Subgrid to Further Drive Transient Inertia Sharing

Fig. 14 shows the experimental results of the hybrid AC/DC/DS MG where y_H is increased to 30. The transient response of DC bus voltage and AC frequency are further optimized. As shown in this figure, the RoCoV of the DC subgrid and the RoCoF of the AC
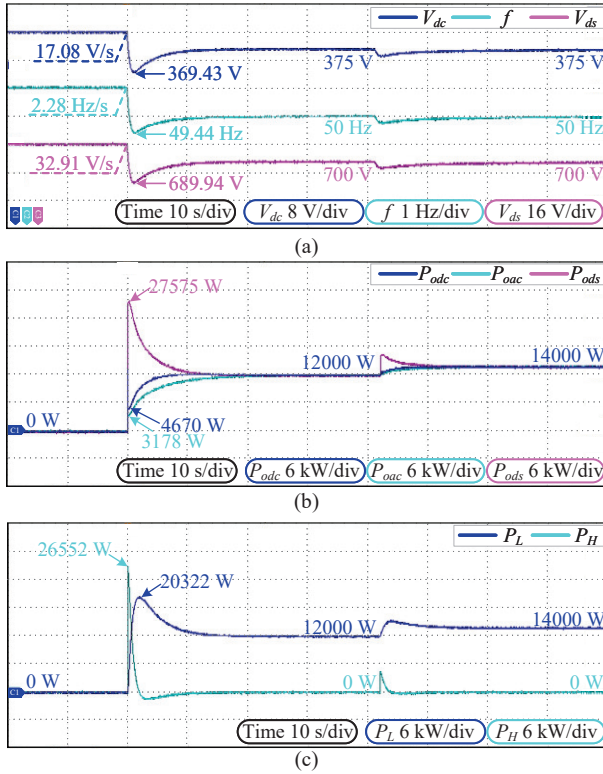
Fig. 14. Response process of hybrid MG with FTS dynamic concatenator and frequency/voltage restoration control. (y_H=30) (a) DC bus voltage and AC frequency response. (b) The output power of DC, AC and DS subgrid. (c) Power allocation of ES_L and ES_H in DS subgrid.

subgrid are reduced to 17.08 V/s and 2.28 Hz/s, respectively, while the nadir of the DC bus voltage and the minimum AC frequency are improved to 369.43 V and 49.44 Hz, respectively. This is because the additional inertia of the DS subgrid is transferred to other low-inertia subgrids through inertia-sharing control, thereby enhancing their transient response characteristics.

In Fig. 14 (b), it can be observed that the increase of y_H does not affect the static global power sharing. Regarding the transient process, the transient power peak of ds subgrid rises to 27.575 kW, while the peak output power of dc and ac subgrids decreases relatively. Owing to the elevated transient power of the DS subgrid and the increase of y_H, the ES_H compensates for a greater proportion of the high-frequency components, whereas the ES_L exhibits a more gradual and stable output as shown in Fig. 14(c). The results demonstrate that increasing ID coefficient of ES_H enables DS subgrid to contribute more effectively to system inertia sharing, thereby alleviating transient power surges in other subgrids. Moreover, a higher y_H improves the DS subgrid's high/low frequency power decomposition. As a result, the transient stress of ES_L is reduced, which in turn prolongs the operational lifespan of the hybrid energy storage system in DS subgrid.

V. CONCLUSION

This paper addresses the challenge of full-time-scale coordinated regulation in hybrid AC/DC/DS microgrids. To this end, a full-time-scale power scheduling strategy for hybrid AC/DC/DS microgrids with dynamic concatenation and autonomous frequency/voltage restoration is proposed, together with an analytical model that characterizes the system's full-time-scale response dynamics. Based on the developed analytical model, simulation, and hardware-in-the-loop experimental results, the proposed strategy is demonstrated to be effective. The FTS dynamic concatenator enables transient inertia transfer among subgrids, thereby enhancing the overall dynamic performance and facilitating a smooth transition toward steady-state global power sharing, ensuring efficient utilization of subgrid capacity. Meanwhile, the autonomous frequency/voltage restoration control successfully eliminates the steady-state deviations induced by conventional virtual inertia, allowing DC and DS bus voltages and AC frequency to autonomously converge to their nominal values, which prevents from severe steady-state offsets that may threaten critical loads or trigger cascading faults. Furthermore, the proposed equivalent circuit model clearly captures the full-time-scale dynamic behavior and inter-subgrid inertia propagation mechanism, providing a novel analytical perspective for coordinated global inertia transfer control.

REFERENCES

[1] F. Yang, X. Feng, and Z. Li, "Advanced microgrid energy management system for future sustainable and resilient power grid," *IEEE Transactions on Industry Applications*, vol. 55, no. 6, pp. 7251–7260, 2019.

[2] M. F. Zia, E. Elbouchikhi, M. Benbouzid, and J. M. Guerrero, "Energy management system for an islanded microgrid with convex relaxation," *IEEE Transactions on Industry Applications*, vol. 55, no. 6, pp. 7175–7185, 2019.

[3] P. Lin, L. Du, H. Zhang, M. Zhu, J. Ma, and P. Wang, "Power lever: To transform interlinking architecture in hybrid ac/dc microgrids community," *IEEE Transactions on Industrial Electronics*, pp. 1–14, 2025.

[4] F. Blaabjerg, R. Teodorescu, M. Liserre, and A. Timbus, "Overview of control and grid synchronization for distributed power generation systems," *IEEE Transactions on Industrial Electronics*, vol. 53, no. 5, pp. 1398–1409, 2006.

[5] C. Jin, P. Wang, J. Xiao, Y. Tang, and F. H. Choo, "Implementation of hierarchical control in dc microgrids," *IEEE Transactions on Industrial Electronics*, vol. 61, no. 8, pp. 4032–4042, 2014.

[6] Z. Zhang, C. Jin, Y. Tang, C. Dong, P. Lin, Y. Mi, and P. Wang, "A modulized three-port interlinking converter for hybrid ac/dc/ds microgrids featured with a decentralized power management strategy," *IEEE Transactions on Industrial Electronics*, vol. 68, no. 12, pp. 12 430–12 440, 2021.

[7] F. Li, J. Zhu, L. Yu, S. Bu, H. Zhao, J. Zhao, Y. Xu, J. M. Guerrero, and C. Wang, "An imbalance-status-enabled autonomous global power-sharing scheme for solid-state transformer interconnected hybrid ac/dc microgrids," *IEEE Transactions on Smart Grid*, vol. 14, no. 3, pp. 1750–1762, 2023.

[8] P. C. Loh, D. Li, Y. K. Chai, and F. Blaabjerg, "Autonomous operation of hybrid microgrid with ac and dc subgrids," *IEEE Transactions on Power Electronics*, vol. 28, no. 5, pp. 2214–2223, 2013.

[9] G.-S. Lee, D.-H. Kwon, S.-I. Moon, and P.-I. Hwang, "A coordinated control strategy for lcc hvdc systems for frequency support with suppression of ac voltage fluctuations," *IEEE Transactions on Power Systems*, vol. 35, no. 4, pp. 2804–2815, 2020.

[10] J. Chen, D. Yue, C. Dou, L. Chen, S. Weng, and Y. Li, "A virtual complex impedance based $p - \dot{V}$ droop method for parallel-connected inverters in low-voltage ac microgrids," *IEEE Transactions on Industrial Informatics*, vol. 17, no. 3, pp. 1763–1773, 2021.

[11] P. C. Loh, D. Li, Y. K. Chai, and F.Blaabjerg, "Autonomous control of interlinking converter with energy storage in hybrid ac–dc microgrid," *IEEE Transactions on Industry Applications*, vol. 49, no. 3, pp. 1374–1382, 2013.

[12] V. Jayan and A. M. Y. M. Ghias, "Computationally-efficient model predictive control of dual-output multilevel converter in hybrid microgrid," *IEEE Transactions on Power Electronics*, vol. 38, no. 5, pp. 5898–5910, 2023.

[13] P. Lin, P. Wang, C. Jin, J. Xiao, X. Li, F. Guo, and C. Zhang, "A distributed power management strategy for multi-paralleled bidirectional interlinking converters in hybrid ac/dc microgrids," *IEEE Transactions on Smart Grid*, vol. 10, no. 5, pp. 5696–5711, 2019.

[14] C. Sulzberger, "Triumph of ac. 2. the battle of the currents," *IEEE Power and Energy Magazine*, vol. 1, no. 4, pp. 70–73, 2003.

[15] Q. Hong, M. A. U. Khan, C. Henderson, A. Egea-Àlvarez, D. Tzelepis, and C. Booth, "Addressing frequency control challenges in future low-inertia power systems: A great britain perspective," *Engineering*, vol. 7, no. 8, pp. 1057–1063, 2021.

[16] C. Li, Y. Li, Y. Cao, H. Zhu, C. Rehtanz, and U. Häger, "Virtual synchronous generator control for damping dc-side resonance of vsc-mtdc system," *IEEE Journal of Emerging and Selected Topics in Power Electronics*, vol. 6, no. 3, pp. 1054–1064, 2018.

[17] "Photovoltaic (pv) systems – characteristics of the utility interface," International Electrotechnical Commission, Geneva, Switzerland, Tech. Rep. IEC 61727, 2004.

[18] P. Lin, Q. Meng, M. Zhu, and F. Blaabjerg, "Dynamic circuit-based unified power regulation for hybrid ac/dc/ds microgrids: A comprehensive approach to static and transient control," *IEEE Transactions on Industrial Electronics*, 2025, doi: 10.1109/TIE.2025.3585029.

[19] Z. Zhang, J. Fang, C. Dong, C. Jin, and Y. Tang, "Enhanced grid frequency and dc-link voltage regulation in hybrid ac/dc microgrids through bidirectional virtual inertia support," *IEEE Transactions on Industrial Electronics*, vol. 70, no. 7, pp. 6931–6940, 2023.

[20] J. Wang, W. Huang, N. Tai, M. Yu, R. Li, and Y. Zhang, "A bidirectional virtual inertia control strategy for the interconnected converter of standalone ac/dc hybrid microgrids," *IEEE Transactions on Power Systems*, vol. 39, no. 1, pp. 745–754, 2024.

[21] P. Lin, C. Jin, J. Xiao, X. Li, D. Shi, Y. Tang, and P. Wang, "A distributed control architecture for global system economic operation in autonomous hybrid ac/dc microgrids," *IEEE Transactions on Smart Grid*, vol. 10, no. 3, pp. 2603–2617, 2019.

[22] P. Wang, C. Jin, D. Zhu, Y. Tang, P. C. Loh, and F. H. Choo, "Distributed control for autonomous operation of a three-port ac/dc/ds hybrid microgrid," *IEEE Transactions on Industrial Electronics*, vol. 62, no. 2, pp. 1279–1290, 2015.

[23] C. Jin, J. Wang, and P. Wang, "Coordinated secondary control for autonomous hybrid three-port ac/dc/ds microgrid," *CSEE Journal of Power and Energy Systems*, vol. 4, no. 1, pp. 1–10, 2018.

[24] P.Kundur, "Power system stability," *Power system stability and control*, vol. 10, pp. 7–1, 2007.

[25] P. Lin, P. Wang, J. Xiao, J. Wang, C. Jin, and Y. Tang, "An integral droop for transient power allocation and output impedance shaping of hybrid energy storage system in dc microgrid," *IEEE Transactions on Power Electronics*, vol. 33, no. 7, pp. 6262–6277, 2018.

[26] P. Yang, M. Yu, Q. Wu, N. Hatziargyriou, Y. Xia, and W. Wei, "Decentralized bidirectional voltage supporting control for multi-mode hybrid ac/dc microgrid," *IEEE Transactions on Smart Grid*, vol. 11, no. 3, pp. 2615–2626, 2020.

[27] T. Dragičević, X. Lu, J. C. Vasquez, and J. M. Guerrero, "Dc microgrids—part i: A review of control strategies and stabilization techniques," *IEEE Transactions on Power Electronics*, vol. 31, no. 7, pp. 4876–4891, 2016.

[28] Texas Instruments, *TMS320F28335 Digital Signal Controller (DSC) Datasheet*, Texas Instruments, Dallas, TX, USA, 2022, [Online]. Available: https://www.ti.com/lit/ds/symlink/tms320f28335.pdf.